RMetS
Royal Meteorological Society

Characteristics and predictability of a supercell during HyMeX SOP1

Mario Marcello Miglietta,[a*] Agostino Manzato[b] and Richard Rotunno[c]

[a]*ISAC-CNR, Lecce, Italy*
[b]*OSMER, ARPA Friuli Venezia Giulia, Visco, Italy*
[c]*Mesoscale and Microscale Meteorology Laboratory, NCAR†, Boulder, CO, USA*

*Correspondence to: M. M. Miglietta, CNR-ISAC, Strada Provinciale Lecce-Monteroni, Lecce 73100, Italy. E-mail: m.miglietta@isac.cnr.it

An analysis is presented here of intense convection affecting the Friuli Venezia Giulia region (FVG, northeastern Italy) during the Intensive Observation Period 2b (IOP2b) in the first Special Observation Period (SOP1) of HyMeX (HYdrological cycle in Mediterranean EXperiment). The present study focuses on the first of three severe-convection episodes that affected FVG on the morning of 12 September 2012. In the first episode, a supercell, which produced hail and severe damage to trees and buildings, was observed on the plain of FVG. The available observations are analysed together with a high-resolution mesoscale model, in order to identify the relevant mechanisms for the formation and development of the cell. Six different simulations were performed starting at three different initial times, using respectively two different analysis/forecasts as initial/boundary conditions. A *large spread* in forecast precipitation is found among the six simulations. Only a few of the simulations were able to reproduce intense rainfall on the plain of FVG during the morning, although with significant differences in the rainfall distribution among them. One of the six simulations well reproduces the observed elongated distribution of the intense rainfall maximum; the characteristics of the cell responsible for this distribution are consistent with those expected for a supercell and its simulated evolution near the Adriatic coast agrees well with the other observations. Some instability parameters over the FVG plain and offshore (over the northern Adriatic Sea) are analysed every 5 min, showing that during this event the potential instability varies significantly over small space and time intervals and among the simulations. The best simulations have the best match to the observed potential instability calculated using the mean characteristics of the lowest 500 m layer.

Key Words: HyMeX; supercells; convection; predictability; instability indices; limited-area model

Received 15 February 2016; Revised 14 June 2016; Accepted 23 June 2016; Published online in Wiley Online Library

1. Introduction

Recent events have made it clear that severe convection is not rare in the Mediterranean region and may sometimes produce significant damage and casualties. For example, on 8 July 2015, an EF4 (Enhanced Fujita Scale 4) tornado struck the area west of Venice, causing one death and 72 injured, while a multi-vortex EF3 tornado affected southeastern Italy on 28 November 2012, causing one casualty and estimated damage of 60 M€ to the largest steel plant in Europe (Miglietta and Rotunno, 2016). The monitoring and prediction of such severe localized convective events requires a deeper understanding of the relevant mechanisms necessary for their development. The present article is a contribution towards this goal.

Routine short-term (0–36 h) numerical weather forecasts of deep convection have existed for about a decade (Weisman *et al.*, 2008). These forecasts strongly rely on mesoscale (O (100–1000 km)) features in the initial condition to predict the location and timing of areas of convection, as well as the type of convection (supercells, squall lines, etc.). The state-of-the-art practice is to use ensembles of such forecasts generated by diverse initial conditions in order to estimate the forecast uncertainty (Schwartz *et al.*, 2015). As the predictability limit for convective-scale elements is at most a few hours (Lilly, 1990), the precise location, timing and type of convection within the mesoscale-model-predicted area is of course not possible. The possibility of making short-term (0–60 min) forecasts using cloud-scale models of severe convection is described in Stensrud *et al.* (2009).

As the studies quoted above are in the context of the physical geography of the USA, the experience gained from them cannot be simply applied to the Mediterranean basin, where the different

†The National Center for Atmospheric Research is sponsored by the National Science Foundation.

physical geography (e.g. the presence of complex orography, coastlines, land–sea gradients of temperature and surface drag) may affect the conditions for the initiation and development of convection.

The Friuli Venezia Giulia region (FVG, northeastern (NE) Italy) has a high incidence of deep convection and thus is a natural laboratory for the analysis of such events. Together with the peak in the average yearly rainfall in the Alpine region (Frei and Schär, 1998; Isotta *et al.*, 2014), a high frequency of thunderstorms (Feudale and Manzato, 2014), hailstorms (Manzato, 2012; Punge *et al.*, 2014), tornadoes and waterspouts (Giaiotti *et al.*, 2007) have been identified in the climatology of FVG; other high-impact events, such as bow-echoes (Pucillo and Manzato, 2010) and heavy rain episodes (Davolio *et al.*, 2016) have also been observed. The frequent occurrence of these events is due to the interplay among frontal systems, orography, and the relatively warm and shallow Adriatic Sea that borders FVG.

For these reasons, FVG was included as a target area both in the Mesoscale Alpine Programme (Bougeault *et al.*, 2001) and in the Hydrological cycle in the Mediterranean Experiment (HyMeX, http://www.hymex.org), first Special Observation Period (SOP1: Ducrocq *et al.*, 2014). In the latter campaign, three severe-convection episodes affected FVG during Intensive Observation Period 2b (IOP2b), on the morning of 12 September 2012. In the first of these episodes, a supercell formed on the plain of FVG and produced hail and severe damage to trees and buildings near the coast. This case is investigated here with a high-resolution numerical weather prediction model to explore the characteristics of the event and the sensitivity of precipitation and of the supercell features to different initial and boundary conditions. Although the physics parametrizations can also influence the simulations, here the schemes are kept fixed for simulations (although some preliminary sensitivity tests have been performed; see section 3).

The article is organized as follows. Section 2 provides a synoptic and mesoscale overview of the event. Section 3 is focused on numerical simulations, including a comparison with the available data (surface-station measurements, satellite-derived winds and radiosonde profiles) and a discussion of the modelling results from a predictability perspective. Section 4 presents the features of the simulated storm, identifying the characteristics typical of supercells. Conclusions are summarized in section 5.

2. Synoptic and mesoscale conditions

A detailed description of the synoptic conditions during IOP2b of HyMeX SOP1 is provided in Manzato *et al.* (2015), hereafter M15; here only a brief summary of the most relevant features is reported. The 500 hPa geopotential height map in M15's Figure 2 shows a diffluent trough, associated with a cold front, moving across western France, from the north Atlantic southeastward on the morning of 12 September 2012. The trough and cold front reach NE Italy in the late afternoon of the same day (Figure 1(a)).

A closer look at the mean-sea-level pressure (MSLP) field in Figure 1(a) shows two small-scale cyclones which help guide warm, moist air to FVG: an orographic lee cyclone in the Gulf of Genoa and another cyclone over the Po Valley. The latter pressure minimum is associated with a low-level cyclonic circulation that straddles the Adriatic coast of FVG. This latter circulation has intense southeasterly winds, which move warm and moist air northward along the east side of the Adriatic and a southwesterly wind that flows downslope across the Apennines. This flow configuration produces an elongated tongue that brings moist air from the sea inland where it is available to feed convection. Further verification of this mesoscale flow pattern is found in the present case by the satellite-retrieved surface wind from the Advanced Scatterometer (ASCAT) at 0839 UTC over the Adriatic Sea (Figure 1(b)).

The 6 h accumulated rainfall from 0600 to 1200 UTC, 12 September in Figure 2 is estimated by the Fossalon di Grado radar using the Marshall and Palmer (1948) equation and corrected with rain-gauge measurements. Intense and widespread precipitation affects the region, with a peak of more than 150 mm in 6 h in the western part of the FVG Prealps, and another band of intense precipitation (estimated at about 75 mm) generated by the supercell, extending from the Veneto region eastward along the coastal regions (near Palazzolo in Figure 2).

The evolution of the atmospheric vertical structure at Udine (46.03°N, 13.18°E), which is near the centre of the FVG plain, shows that several features conducive to intense convection occur on the morning of 12 September (Figure 3). First, a southeasterly low-level jet of moist and warm air between 400 and 1400 m above mean sea level (amsl) at 0600 UTC, which is responsible for the high values of equivalent potential temperature ($\theta_e > 330$ K) in the lower troposphere. The latter feature, combined with colder θ_e-air advection at middle levels (see the slope of the black isotherms between 4 and 7 km amsl), produce conditions of potential instability, increasing the value of convective available potential energy (*CAPE*) to approximately 2000 J kg^{-1}. At the same time, weak convective inhibition (*CIN*) makes the environment favourable to the triggering of convection. An increase of the vertical wind shear is also apparent, due to the intensification of the upper-level wind and the rotation of the low-level wind from westerly to easterly. Such unstable conditions are then quickly eliminated by the entrance of much colder air associated with a frontal system in the afternoon of 12 September.

The transit of cloud systems across the region and the triggering of convection can be identified in M15's Figure 4, where images from the European Organisation for the Exploitation of Meteorological Satellites (EUMETSAT) experimental 2.5 min rapid scans from the High Resolution Visible channel of Meteosat Second Generation are shown. At around 0630 UTC, 12 September, M15's Figure 4 shows the first convective cell is triggered in the Alpine foothills, in the western part of the FVG region, where the 6 h accumulated rainfall maximum of 150 mm is observed. The radar data presented here in Figure 4 shows that, in the next 1.5 h, the 'northern storm' (as referred to in M15) intensifies approximately in the same location. In the following hour, a new cell, the 'southern storm', develops and grows rapidly.

The evolution of the two cells is clearly identified in detail in Figure 4. The radar reflectivity maps indicate the triggering of the southern cell near the Adriatic Sea at approximately 0740 UTC (not shown) and its subsequent northeastward movement (shown in Figure 4 between 0810 and 0830 UTC). Since the environmental wind is westerly and this cell moves to the left of the flow, it is the 'left mover' of a previous supercell split (Weisman and Klemp, 1982), as also suggested by radar data. From the analysis of M15 (their Figure 13), the northern storm is also very likely a supercell. When the two (probable) supercells get closer to each other at about 0830 UTC, the southern storm is able to intercept the moist low-level air (Figure 1(b)) that had been feeding the northern storm, so that the latter suddenly dissipates (Figure 4). Finally, the remaining cell deviates eastward along the coast, where it exhibits supercellular features, such as the hail reported in Latisana and the intense downdraught/outflow in Palazzolo at about 0900 UTC (Figure 4). Later on, the system moves along the coast evolving into a bow-echo pattern, as shown in M15's Figure 5(d).

The different evolution of θ_e observed at four surface stations, whose locations are shown in Figure 2, is stressed in Figure 5. While Udine, which is north of the area of main convective activity, shows small variations of θ_e, the other three stations exhibit very sharp drops corresponding to the storm passage. Such large drops in θ_e suggest a strong efficiency of the storm in converting the environmental thermodynamic energy into precipitation and kinetic energy.

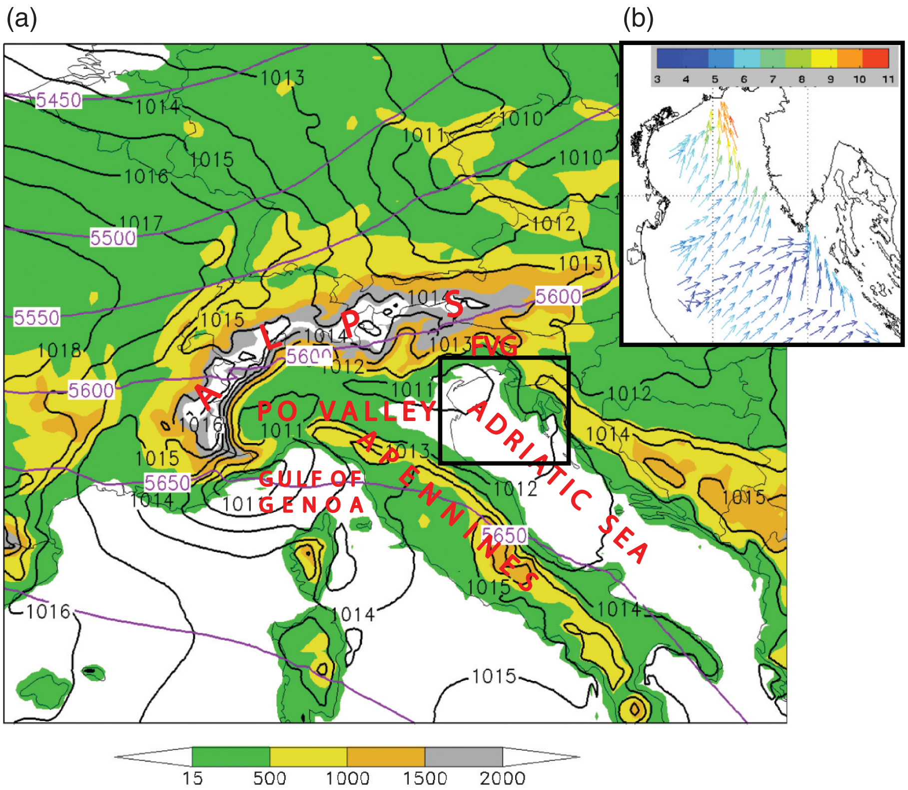

Figure 1. (a) 500 hPa geopotential height (gpm; light lines) and mean-sea-level pressure (hPa; dark lines) at 0600 UTC 12 September 2012, from the ECMWF forecast (initial time 0000 UTC 12 September 2012) (Courtesy of Arturo Pucillo, OSMER – ARPA FVG); (b) wind data (m s^{-1}) from MetOP-ASCAT scatterometer (12.5 km horizontal resolution) at 0839 UTC 12 September (Courtesy of Stefano Zecchetto, ISAC-CNR). The locations of the places mentioned in the text are shown in (a), and the box in (a) corresponds to the domain shown in (b).

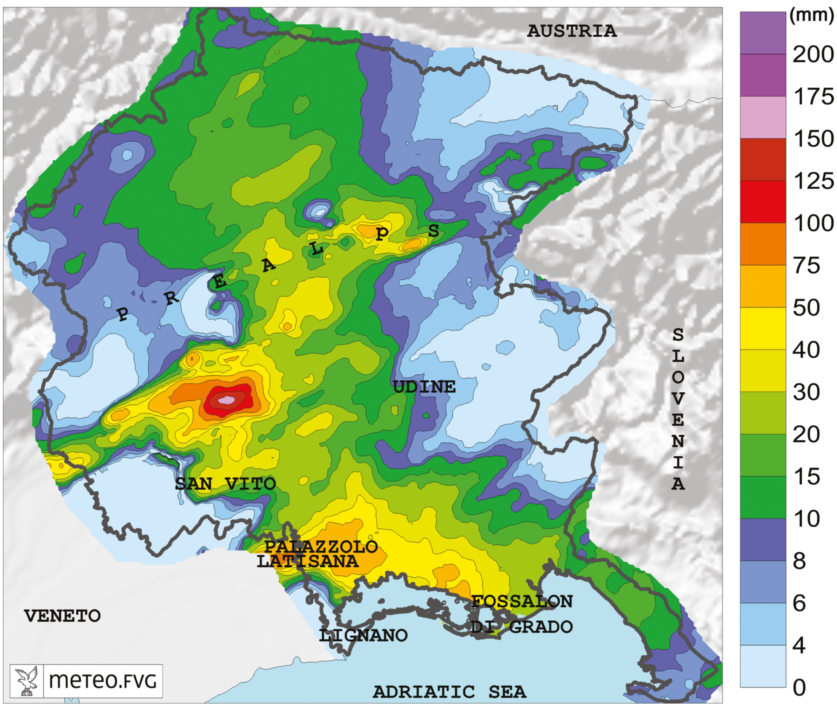

Figure 2. FVG 6 h accumulated rainfall (mm) in the period 0600–1200 UTC 12 September 2012 (six-level radar data corrected with rain-gauge observations). (Courtesy of Andrea Cicogna, OSMER - ARPA FVG).

3. Numerical simulations

3.1. Simulations with WRF model

The supercell described above is analysed here by means of numerical simulations performed with the Weather Research and Forecasting (WRF) model, version 3.5.1 (see http://www.wrf-model.org: Skamarock *et al.*, 2008). WRF is a state-of-the-art weather prediction system that solves the fully compressible, nonhydrostatic equations of atmospheric motion. Forty terrain-following hydrostatic-pressure vertical levels are used in the present simulations, their vertical distance ranging from 58 m in the boundary layer to 600 m in the lower stratosphere. In order to analyse the detailed evolution of the meteorological parameters, model output is saved every 5 min.

The model is implemented using three different one-way-nested grids, with horizontal spacings respectively of 9, 3 and 1 km, extending for 190 (in the east–west direction) × 150 (in the

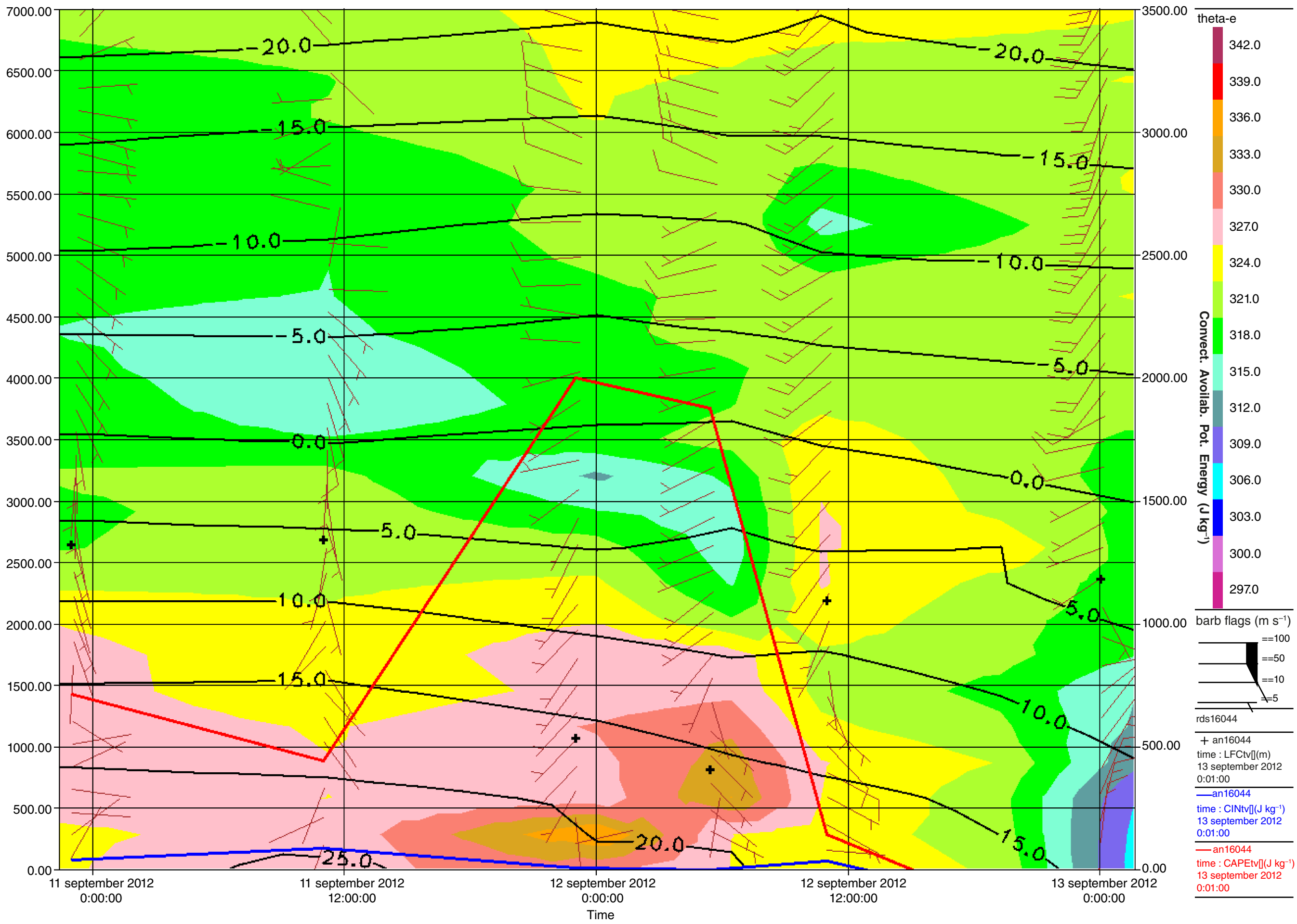

Figure 3. Vertical–time series in the layer 0–7000 m amsl (left scale) of soundings at the location of Udine sounding station (46.03°N, 13.18°E) from 1200 UTC 11 September to 0000 UTC 13 September 2012, with horizontal winds (barbs) and θ_e (bar scale). Superimposed are estimates of *CAPE* (light line) and *CIN* (dark line without contour labels) – the scale of these two parameters is on the right vertical axis-, *LFC* (Level of Free Convection) ('+' signs), and temperature (black contours). Observed soundings are reported every 6 h between 0000 UTC 12 September and 0000 UTC 13 September, due to the request of two additional soundings at 0600 and 1800 UTC (note that the wind at 1800 UTC is not shown because it was not recorded correctly).

north–south direction) grid points in the outer grid, 271 × 163 in the middle grid and 181 × 181 in the inner grid (Figure 6). The area of interest is in the centre of the inner domain and on the eastern side of the two outer domains, in order to properly represent the large-scale evolution of the trough, which propagates from the west.

Since the predictability of the event is the main subject of the present article, different initial/boundary conditions are considered to force the simulations. In particular, the European Centre for Medium-range Weather Forecasts (ECMWF) and the Global Forecasting System (GFS) analyses are used as initial conditions. The boundary conditions are updated every 3 h with the ECMWF Integrated Forecasting System (IFS) and GFS forecasts; thus the simulations are performed in an operational-like configuration. Also, different starting times have been tested to initialize the model simulations, respectively 0000 and 1200 UTC, 11 September 2012, and 0000 UTC, 12 September 2012. Simulations are named according to the initial time, for example the run forced with GFS data starting at 1100 UTC, 12 September, is named as GFS1112. As will be shown, GFS1112 is the simulation that best reproduces the observed evolution of the supercell, hence it is considered the 'control run' hereafter.

Preliminary experiments were undertaken to identify an optimal set of parametrizations, able to better reproduce the cell evolution. Following the outcome of these experiments, the model is implemented with the following schemes: Thompson *et al.* (2008) microphysics; Rapid Radiative Transfer Model (RRTM) for long-wave radiation based on Mlawer *et al.* (1997) and Dudhia (1989) for short-wave radiation; the unified Noah land-surface model (Niu *et al.*, 2011); Mellor–Yamada–Janjic planetary boundary layer (Janjic, 2001). Thus, the schemes are the same as those employed for the simulations with the WRF model in M15. Since the large-scale forcing is the same, the better result of the GFS1112 run in reproducing the supercell evolution compared to the simulation in M15 indicates the importance of domain sizes (which are larger in the present study) and, mainly, of the fine horizontal resolution required for a realistic simulation of meso-γ scale features.

There is no consensus on the use of convection parametrization for grid spacing slightly smaller than 10 km, as in the outer domain used here. Done *et al.* (2006) reported on cases of fairly intense convection with mesoscale organization, showing there is no advantage of using a cumulus parametrization even for grid spacing slightly larger than 10 km. In the present study, no cumulus scheme is used in any domain. In order to see how this choice affects the simulation, an additional run was performed, using the same configuration as GFS1112, but switching on the Kain (2004) cumulus convection scheme in the outer grid and leaving the explicit treatment of convection only in the two inner domains.

Additionally, different schemes for the planetary boundary layer (PBL) have been tested; we believe that the PBL parametrization plays a key role in the present case-study by modifying the characteristics of the atmosphere in the low levels, thus the instability properties and the flow dynamics. In both cases, differences of the simulations with the GFS1112 run are relatively minor compared to those emerging among experiments with different initial times and/or large-scale forcing: they show the same solution characteristics, with only slight modifications in the rainfall amount and distribution. As a consequence, hereafter the predictability analysis will focus on the sensitivity

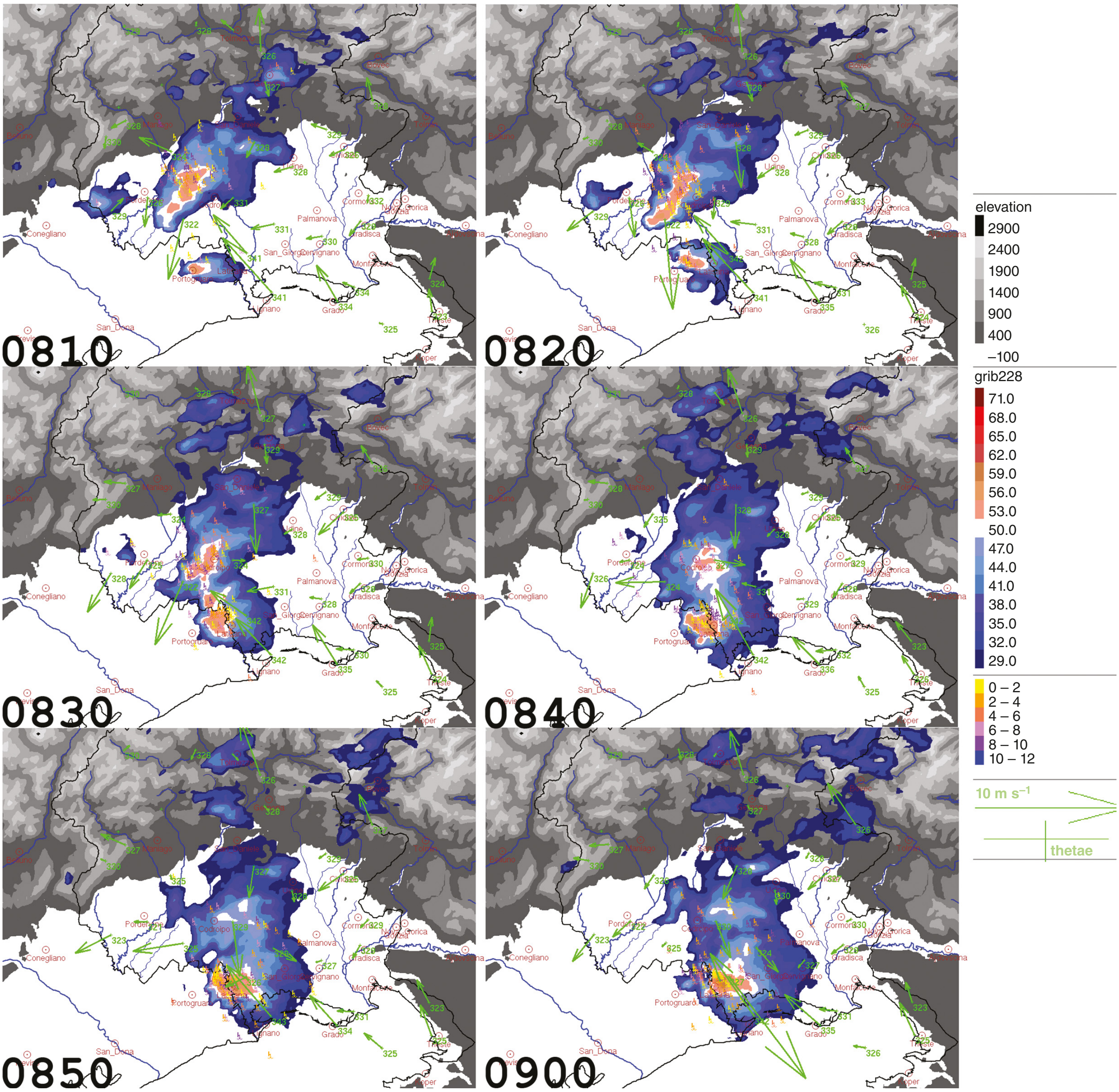

Figure 4. Vertical Maximum Intensity (VMI) of the reflectivity (dBZ; shaded; grib228 bar) measured by the Fossalon di Grado radar at 0810, 0820, 0830, 0840, 0850 and 0900 UTC, 12 September 2012, with equivalent potential temperature (θ_e in K; numbers) and 10 m wind (m s^{-1}; arrows) observed by surface stations 5 min later and CESI (Centro Elettrotecnico Sperimentale Italiano) cloud-to-ground lightning (strokes; lower bar) ±6 min around the nominal time. Mountain elevation is shown with the elevation bar.

to different initial/boundary conditions without considering the role of parametrization schemes.

3.2. Mesoscale and precipitation patterns

In M15, both models (MOLOCH and WRF) used for the simulation of the event were able to reproduce the triggering of convection over the foothills of the Alps. Also, they simulated some mesoscale features that possibly played a key role during this phase, such as the tongue of warm air advected by an intense low-level jet. However, both models missed the exact timing, location and movement of the cells. Thus, although both models captured the mesoscale environment fairly well, they were far from being an accurate simulation of the convective system.

In order to better explore this point, six experiments were performed with the WRF model using different initial and boundary conditions, as discussed in section 3.1. The characteristics of the low-level inflow of warm, moist air at 0600 UTC are shown in Figure 7 for all runs. The simulations show that important mesoscale differences near the mountains and over the plain are already present before the triggering of convection near the foothills. Thus, the discrepancies growing from initial small-scale differences spreading upscale as a consequence of moist convection (Zhang *et al.*, 2002, 2003) probably have a minor effect here.

The ECMWF runs (Figure 7, right) all show a similar pattern at 0600 UTC: the warm-air tongue penetrates inland, although with a different northward extent and intensity (the earlier the starting time, the cooler the air and the narrower the jet), while the cold air always remains confined near the mountains and the foothills. The differences among the GFS-forced runs are more apparent (Figure 7, left). The GFS1200 run shows a peculiar configuration, since it is characterized by a wide area of very cold, low-level air, extending from the mountains to the sea, while the warm tongue is confined to a very narrow region close to the coast.

Compared with the ECMWF simulations, in the GFS1100 and GFS1112 simulations the cold air shows a similar southward extent near the foothills, but is somewhat cooler. Also the inland

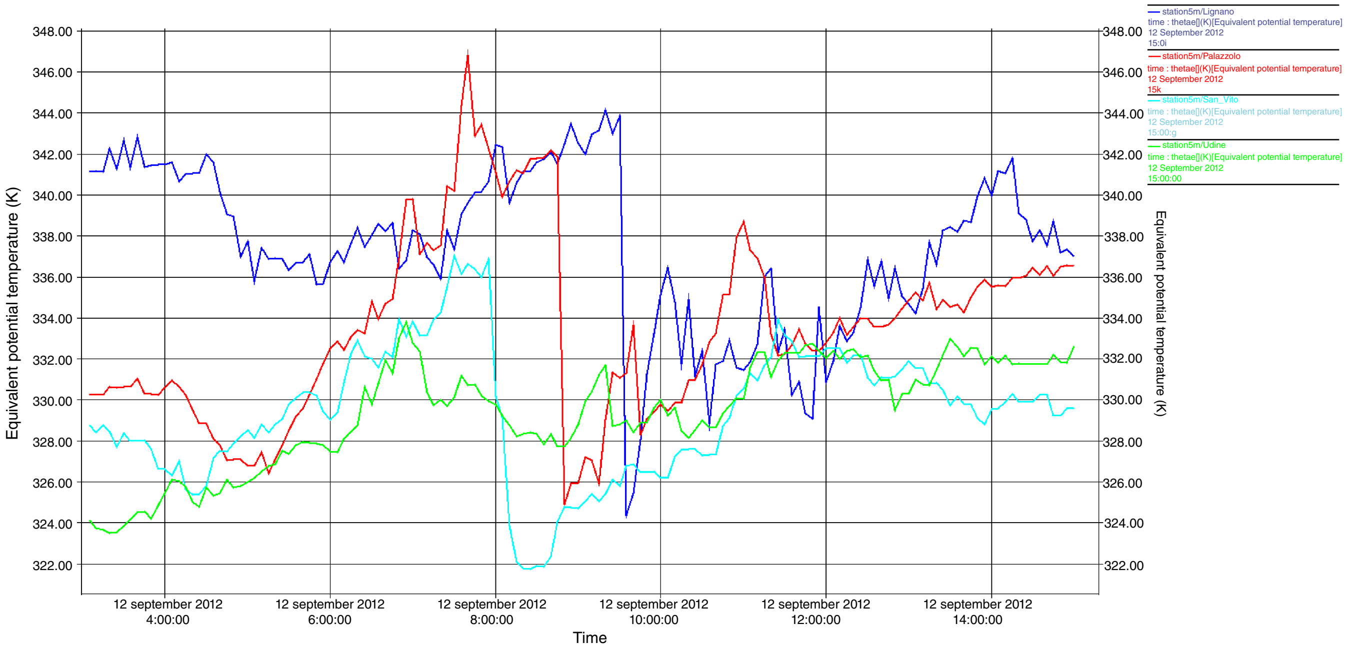

Figure 5. Equivalent potential temperature (θ_e) every 5 min observed in San Vito (cyan), Palazzolo (red), Lignano (blue) and Udine (green) between 0300 and 1500 UTC, 12 September 2012.

penetration of the warm air is much farther, with values close to 340 K simulated even near the foothills (in particular in GFS1112), and shifted farther to the west than in the other runs. The westward deflection of the warm air in its northern tip can be probably attributed to the cyclonic circulation around the pressure meso-low in the Po Valley (Figure 1), centred near Venice, which appears slightly deeper in the GFS1112 run than in the other runs. *This feature plays an important role in favouring supercell development since it prevents the warm tongue from moving eastward, forcing it to remain in the vicinity of the foothills.* Between the two experiments, GFS1112 has a much farther penetration inland, and a stronger and more extensive low-level jet than GFS1100.

As a consequence of the variety in the simulated mesoscale patterns, there is a large variation in the way the flow interacts with the orography and in the simulated precipitation. To summarize the differences among the simulations, the 6 h accumulated precipitation from 0600 to 1200 UTC is compared in Figure 8. Only the GFS runs and the ECM1200 run are able to reproduce intense rainfall in the FVG plain and the coastal area, although with significant differences in its distribution. Similarly, the variation of maximum updraught vertical velocity with time (not shown) is characterized by a strong variability.

Two experiments shown in Figure 8, ECM1100 and ECM1112, produce precipitation mainly in the northeastern part of the region, near the border with Slovenia, in an area where the observed precipitation is much smaller (cf. Figure 8 with Figure 2), while no precipitation is simulated near the coast. In these two cases, the warm tongue is advected too far north at later times, while the cold air remains confined very close to the mountains (not shown); thus the direct orographic uplift is mainly responsible for rainfall in these runs.

The other experiment forced with ECMWF data (Figure 8(f)) reproduces an intense rainfall peak in the area affected by the supercell, but the simulated precipitation is about 200 mm, about twice that observed (and about the sum of the rainfall maximum in the northern and southern storms). The coastal rainfall is produced – as in the GFS experiments – at the northern terminus of the low-level warm inflow, which remains quasi-stationary near the coast for several hours (not shown). The peak in vertical velocity is above 20 m s^{-1} for a few minutes, but the cell does not show the rotation typical of supercells. Two minor rainfall peaks are also simulated, one in the northeastern region, and another one (corresponding to the observed maximum) near the foothills at the border with Veneto region, but they are significantly underestimated and shifted northward.

The simulated precipitation in the GFS1200 experiment in Figure 8 is also very different from the observations. Some orographic precipitation is again shown near Slovenia, while a rain band is elongated from the west side of the region to the east, following the eastward movement of the northern end of the warm tongue in the morning of 12 September. However, the timing is incorrect, the precipitation is shifted to the north (cf. Figure 8 with Figure 2) and the intensity is significantly underestimated.

The other two GFS-forced experiments in Figure 8 better simulate the observed precipitation. Both experiments, in particular GFS1112, show a persistent vertical velocity larger than 20 m s^{-1} lasting for more than 1 h (not shown). Also, the two simulations are the only ones that produce some rainfall in the northern part of the region near the Alps, in agreement with the observations. The GFS1100 run reproduces fairly well the rainfall amount associated with the supercell near the coast, although the affected region has a shorter east–west extent than that observed, due to the earlier weakening of the supercell. Finally, the GFS1112 run reproduces well the observed elongation of the intense rainfall maximum toward Slovenia, and the precipitation amount is close to the observed. The observed maximum in the foothills is well captured in the simulation, although separated into two distinct and weaker maxima. The presence of the mountains in Slovenia seems to prevent a longer duration of the supercell, which lasts for about 1.5–2 h (in agreement with the analysis in M15's section 5). Markowski and Dotzek (2011) suggested that the reduced humidity in the lee of the mountains has the effect of increasing convective inhibition and is detrimental to supercell development.

Apparently, the successful simulation required a farther inland penetration and a cyclonic rotation of very warm, moist air on the west side of the FVG plain, which is accomplished only in the GFS1100 and GFS1112 experiments (Figure 7). The differences among the simulations evolve from different large-scale initial conditions. Comparing for example ECM1112 with GFS1112 at their (common) initial time, one can see that differences in the initial forcing are relevant especially at low levels. In the latter experiment the pressure low in the Po Valley is deeper, thus a more intense pressure gradient has a more pronounced cyclonic circulation, affecting the inflow of high-θ_e air toward the eastern Po Valley. Small-scale variations in θ_e are known to affect the potential instability of parcels in the layer where convection

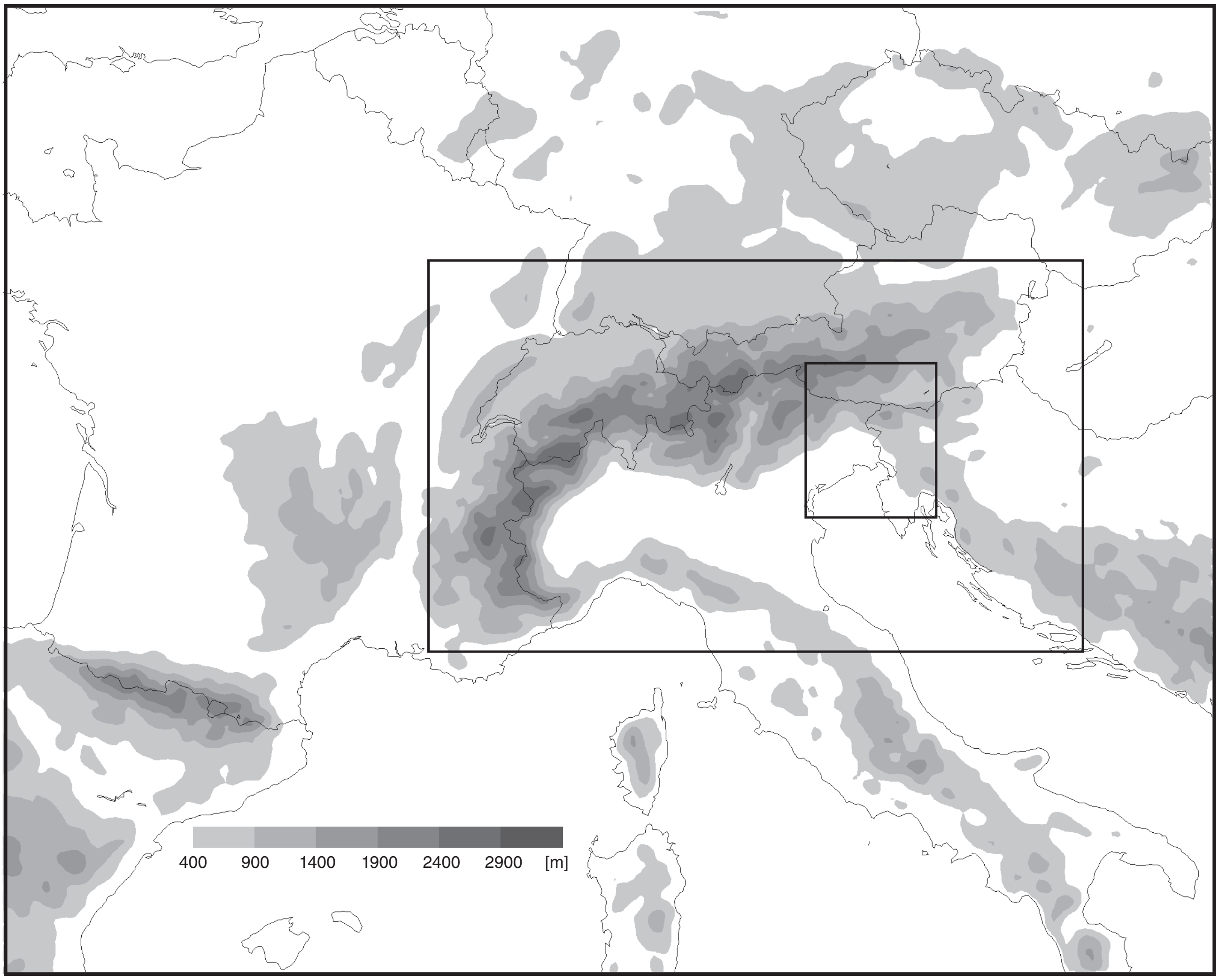

Figure 6. Model grids and topography.

originates (Done *et al.*, 2012). The presence of high-θ_e values at low levels is required to make the atmosphere more unstable and allow for the triggering of *convection near the foothills, which*, as shown in section 4, *leads to the cold-air outflow that plays an important role in the later evolution of the storms.* (Note that the strong gradient of θ_e corresponds to an area of low-level convergence between the southerly inflow and a northeasterly 'barrier wind' from the Alps, which affects the pre-Alpine region and the northern part of the Po Valley, as discussed in M15 and Davolio *et al.* (2016), and favours convective triggering.)

Initially, intense precipitation (larger than 40 mm h^{-1}) in the GFS1112 run (Figure 9) is triggered near the rainfall maximum observed in the foothills (Figure 2). This is an area where *CIN* is low (below 20 J kg^{-1}) and bordered on its southern side by a band of high *CAPE* (above 1500 J kg^{-1}), which was 'advected' northward on the morning of 12 September, through the advection of the high θ_e air at low levels. The simulated soundings near the foothills show that the advection of low-level moisture dramatically increases the instability of the environment in that period. For example, at the point (46.0°N, 12.75°E), the *CAPE* is about 350 J kg^{-1} and *CIN* is -25 J kg^{-1} at 0300 UTC; after 3 h, an increase in the mixing ratio of about 2 g kg^{-1} at the level of the most unstable parcel (950 hPa), produces an increase in θ_e from 329 to 336 K and reduces the inhibition while the *CAPE* increases up to about 1400 J kg^{-1}. Changes in the upper-level profiles, due to the incoming trough, appear as relatively minor in this stage.

3.3. *Simulated and observed vertical profile and instability indices*

The time evolution of the atmospheric profiles simulated at the grid point closest to Udine in the GFS1112 run is shown in Figure 10. Since the time resolution of the model output is 1 h, the rapid changes in the meteorological fields can be detected with greater detail than in the observed time evolution (Figure 3).

The vertical structure of the equivalent potential temperature at Udine, simulated by the model, appears consistent with the observed evolution (cf. Figure 10 with Figure 3). In particular, the GFS1112 run correctly represents the arrival of cold, dry air at mid-levels, the presence of low-level high-θ_e air, the large instability (high *CAPE*) in the early morning of 12 September, the rotation of the wind vector in the low levels along with the intensification of the wind speed in the upper levels and the transit of the cold front in the evening. However, the evolution in the simulation occurs a few hours earlier than in the observations. Compared to Figure 3, the more-frequent model output in Figure 10 shows the presence of high-θ_e air extending from the ground to the upper troposphere corresponding to the development of deep convection, simulated both in the morning and afternoon of 12 September.

One of the main aspects that influence the predictability of this event is the models ability to simulate the vertical structure of the temperature, humidity and wind, which determine potential instability and type of convection (e.g. supercells, multicells, etc.). In order to compare the potential instability and wind profiles among the simulations, as well as with the observed values, sounding-derived and model-derived indices are calculated (Manzato, 2008), before and during the convection. Four instability indices are calculated for all six runs to represent the evolution on the morning of 12 September. On the right side of Figure 11 both the observed values (cross marks) derived from the Udine radiosondes (46.03°N, 13.18°E) and the simulated values every 5 min are shown. On the left side of Figure 11, the

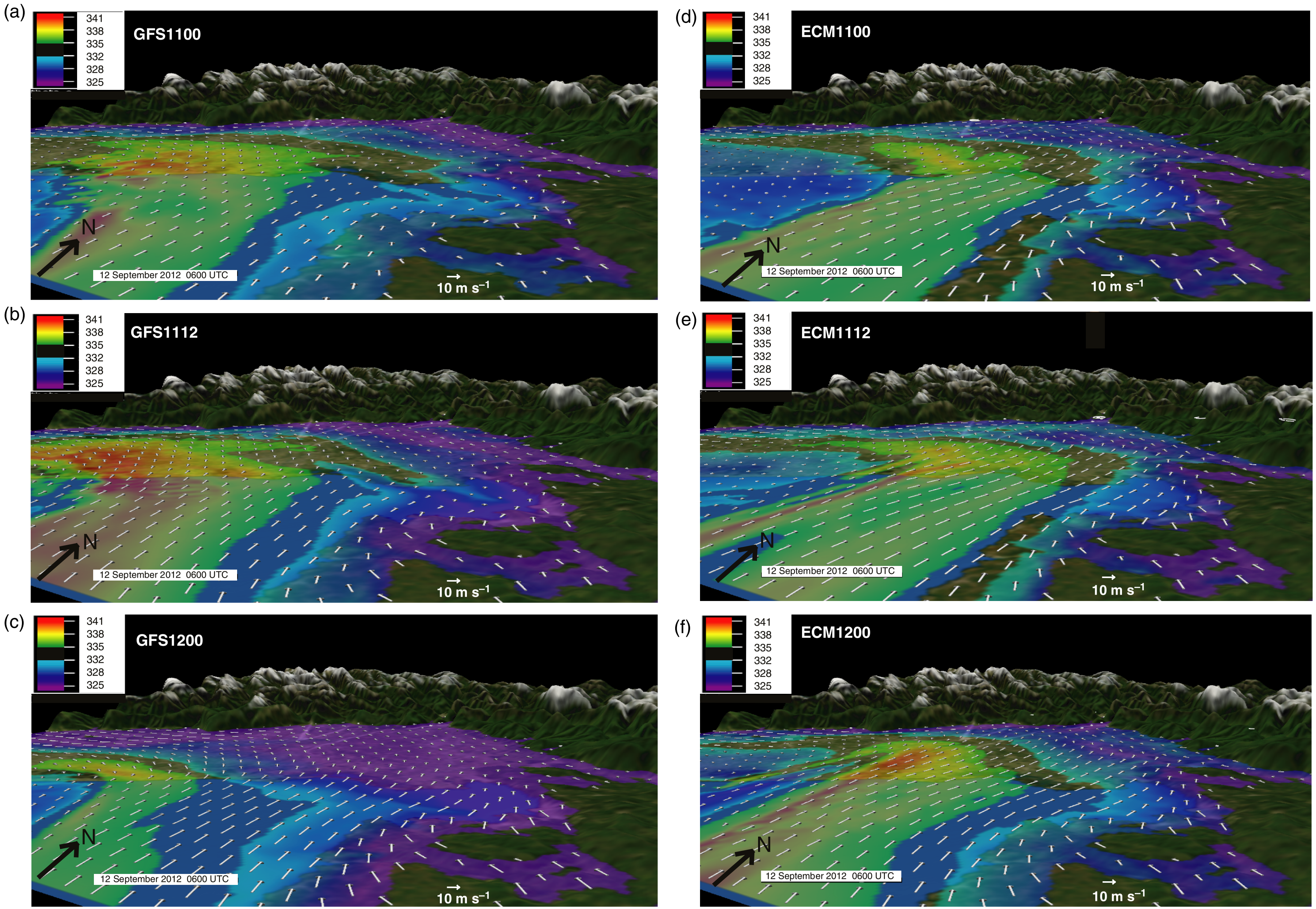

Figure 7. Wind vectors at 350 m height (white arrows), θ_e at 300 m (shaded, for clarity no data shown between 332 and 335 K) at 0600 UTC, 12 September 2012, from GFS runs initialized at (a) 0000 UTC 11 September, (b) 1200 UTC 11 September, (c) 0000 UTC 12 September and from ECMWF runs initialized at (d) 0000 UTC 11 September, (e) 1200 UTC 11 September, (f) 0000 UTC 12 September 2012.

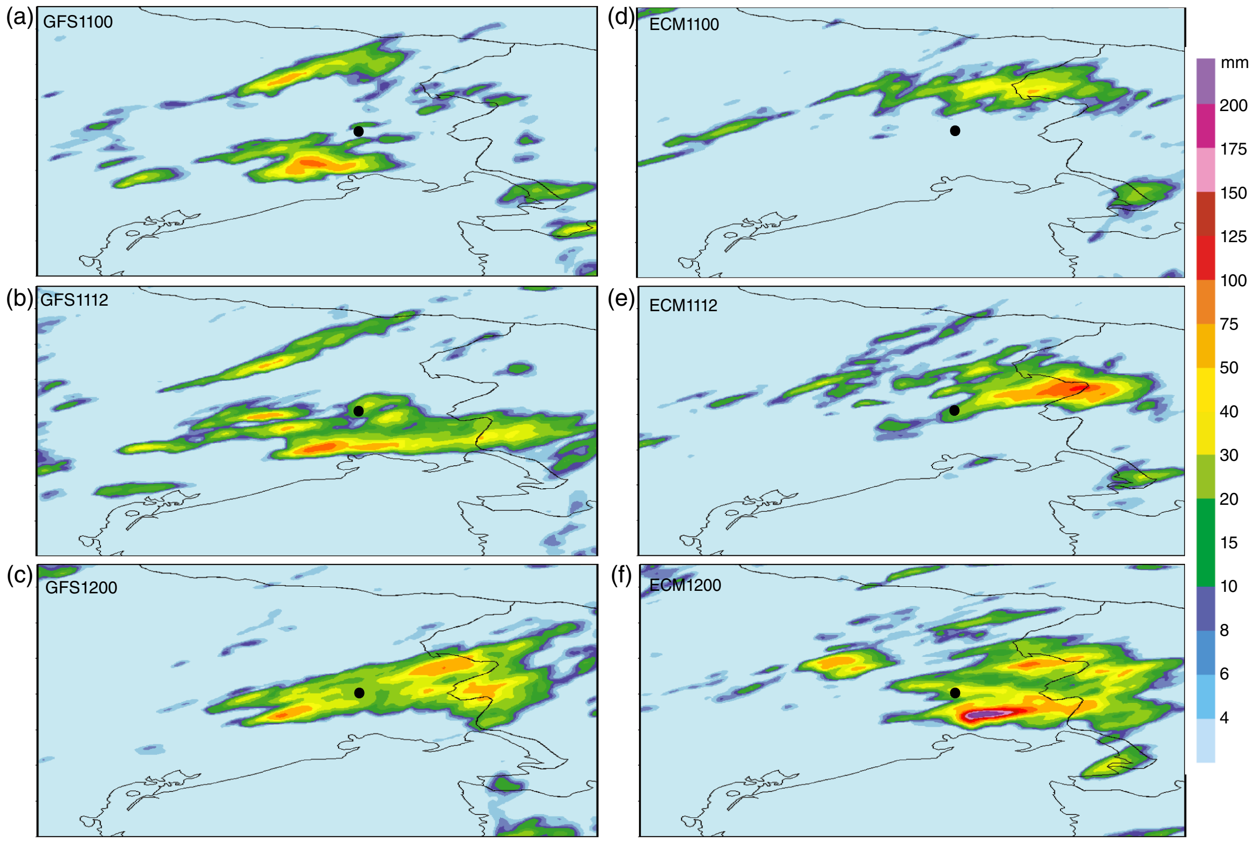

Figure 8. Six-hour rainfall simulated (WRF inner grid) from 0600 to 1200 UTC, 12 September 2012, from GFS runs initialized at (a) 0000 UTC 11 September, (b) 1200 UTC 11 September, (c) 0000 UTC 12 September and from ECMWF runs initialized at (d) 0000 UTC 11 September, (e) 1200 UTC 11 September, (f) 0000 UTC 12 September 2012. The location of the Udine sounding station is shown with the black point.

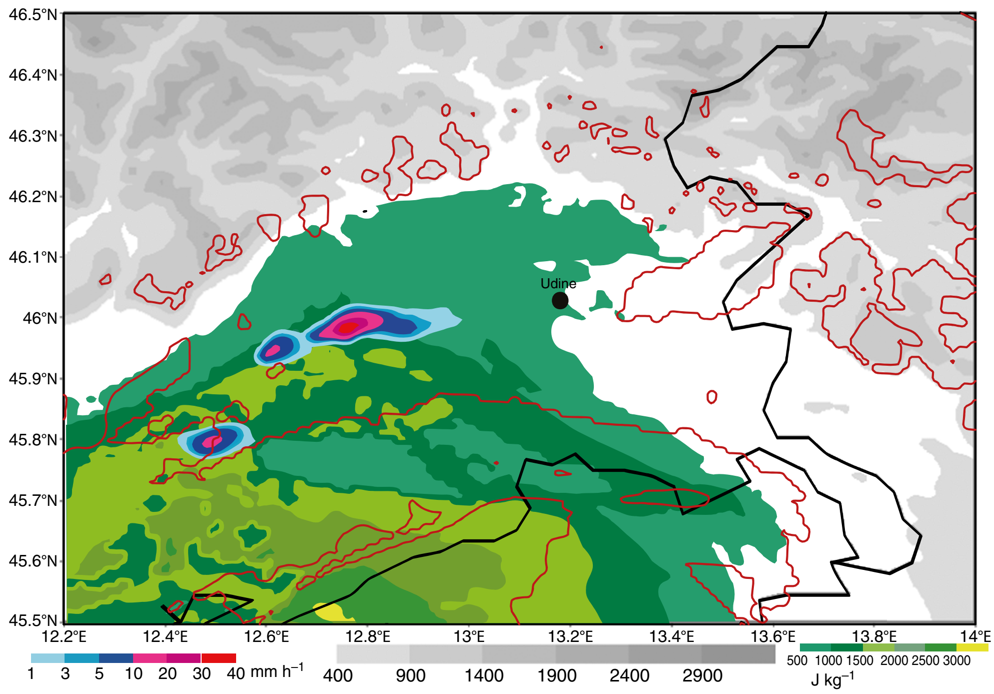

Figure 9. *CAPE* (shading; right-side bar) and *CIN* (light contour = $-20\,\mathrm{J\,kg^{-1}}$) at 0600 UTC 12 September 2012; hourly rainfall (shading; left-side bar) at 0700 UTC. The orography (m) is in grey tones. The location of the Udine sounding station is shown with the black point.

simulated indices are shown at a grid point located offshore over the Adriatic Sea (45.4°N, 13.0°E). All these indices are computed with the 'T_v method' described in Manzato and Morgan (2003), which uses also the 'virtual correction' suggested by Doswell and Rasmussen (1994). Moreover, a centred moving average of three points (10 min of time interval) has been applied to smooth the fast varying indices; even so, the time evolution is very fast, with the indices over land having much sharper fluctuations than those offshore.

The classical Lifted Index (*LI*: Galway, 1956), which uses as the initial parcel the mean air properties in the lowest 500 m, is much larger offshore (*LI* in the range −5 to −8 °C) than over land (*LI* from 0 to −4 °C) between 0500 and 0800 UTC (Figure 11(a)). In the GFS runs, the model-derived *LI* is closer to the observed values in Udine, in particular at 0535 UTC. However, the Lifted Index using the most unstable parcel method (*MUP*, not shown), in which the initial parcel corresponds to the maximum θ_e in the lowest 250 hPa, shows that ECMWF runs have a better estimate

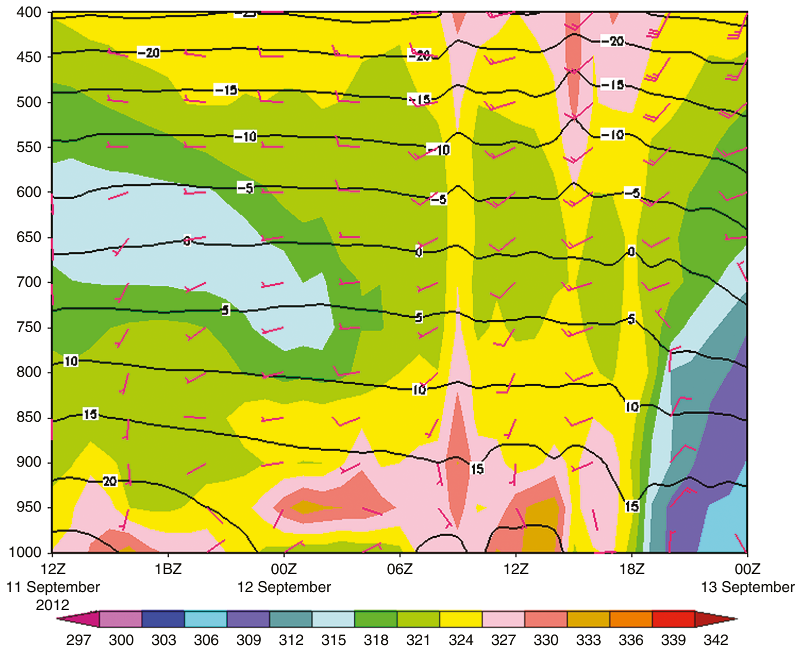

Figure 10. As Figure 3, but for GFS1112 simulated soundings at the location of the Udine sounding station (46.03°N, 13.18°E). Temperature (°C) and θ_e (K) are shown every hour, with horizontal winds every 6 h. The left vertical scale refers to pressure (hPa).

of *LI* using *MUP*, due to its better estimation of the maximum θ_e in the lowest 250 hPa (Figure 11(b)), which is located *above* 500 m. In conclusion, it seems that potential instability based on the lowest 500 m is better described by GFS, while that based on the most unstable parcel (located at higher levels) is better described by ECMWF. The fact that GFS1112 better reproduces the observed dynamics and the precipitation indicates that the potential instability based on the very low levels (lowest 500 m) is the most important to be well predicted in this case.

The sounding-derived maximum θ_e at 0535 UTC is higher than the highest simulated θ_e, while the observed maximum θ_e at 1105 UTC is slightly lower than the lowest simulated θ_e (Figure 11(b)). This means that the drop of almost 10 K in air mass between 0535 and 1105 UTC is underestimated by all six models (similar conclusions can be drawn for the sudden drop of 20 K observed at the surface in Figure 5). Consistent with the *LI*, the simulated maxima of θ_e have much higher values offshore than inland (Figure 11(b)). This very strong north–south gradient of θ_e across the coast is very significant considering that the two locations are only 70 km apart. The feature of the simulations corresponds well with the surface observations, as the value of θ_e in Udine is on average 10 K lower than it is in Lignano before storm passage (Figure 5). This observation means that the very warm, moist air remains confined mainly near the coast, in the west part of FVG.

The fast variations in the simulated Udine indices can be attributed to sudden changes in the northern extent of the low-level jet, probably associated with the movement of the convective cells along the region, which may temporarily block the southerly inflow of warm and moist air. Figure 11(c) shows the meridional component of the mean wind in the lowest 500 m (*LLWv*, with positive values indicating southerly flow). We see that, while a weak southerly component (from about 0 to 4 m s^{-1}) is simulated for most of the time in Udine, for a short period the wind becomes northerly in some runs (GFS1100, GFS1200, ECM1200), due to the outflow associated with the northern storm (Figure 4).

LLWv in the point offshore (Figure 11(c)) is southerly for all time and all runs, apart from ECM1100, and shows a progressive intensification of its magnitude until about 9 m s^{-1}, followed by a sudden drop (occurring between 0730 and 0830 UTC, depending on the model), as to track the passage of a low-level jet. This is in agreement with the presence of a southerly low-level jet over the Adriatic Sea, observed at 0839 UTC in Figure 1(b). The *LLWv* drop is less pronounced in the three GFS runs than in the remaining two ECMWF simulations, hence GFS runs are more efficient in pushing the high-θ_e air of the lowest 500 m from the sea inland.

Lastly, the storm-relative helicity (*SRH*, Figure 11(d)), which is calculated in the lowest 3 km considering the simulated eastward storm speed of 7 m s^{-1}, is evaluated to estimate the potential for the rotation of the cyclonic updraught. The simulations are in good agreement with observations, in particular GFS1112 and GFS1200 (note also that the values for the GFS1112 run are the highest in the point offshore). The parameter shows intense fluctuations inland; offshore the peak occurs a couple of hours earlier (between 0700 and 0800 UTC, depending on the model run). In contrast with most of the other indices, the peaks of this parameter are much higher inland than offshore, probably due to the much stronger wind shear brought about by larger drag over land, in particular in the presence of complex orography. Simulated values of helicity higher than 100 m^2 s^{-2} in Udine occur in all models, denoting a larger potential for cyclonic updraught rotation inland. For example, Manzato (2003) found that, in 1229 cases reporting lightning in FVG in 6 h time-slots, the median of the *SRH* distribution was 29 m^2 s^{-2}, while only 5% of the distribution had *SRH* as high as 174 m^2 s^{-2}. Hence, the simulated value of more than 100 m^2 s^{-2} is toward the upper tail of the local distribution. The increase in this index reflects the larger vorticity advection associated with the cold front and the upper-level trough approaching from the northwest.

In conclusion, from this analysis we have learned that, at least in this case, a more realistic simulation of the lowest levels (both in terms of θ_e and wind structure) seems to have a strong influence on the better predictions of some forecasts with respect to others.

4. Supercell features

In the present section, the characteristics of the cell generated by the merging of the northern and southern storm are analysed and compared with the classical supercell conceptual model. Thus, the three-dimensional structure of the flow around the simulated supercell is investigated more deeply. In the following, only the GFS1112 run, which reproduces better the observed 6 h accumulated rainfall, is considered.

Following Rotunno and Klemp (1985), two distinctive features are recognized as hallmarks of supercell thunderstorms: the propagation to the right of the mean tropospheric wind shear

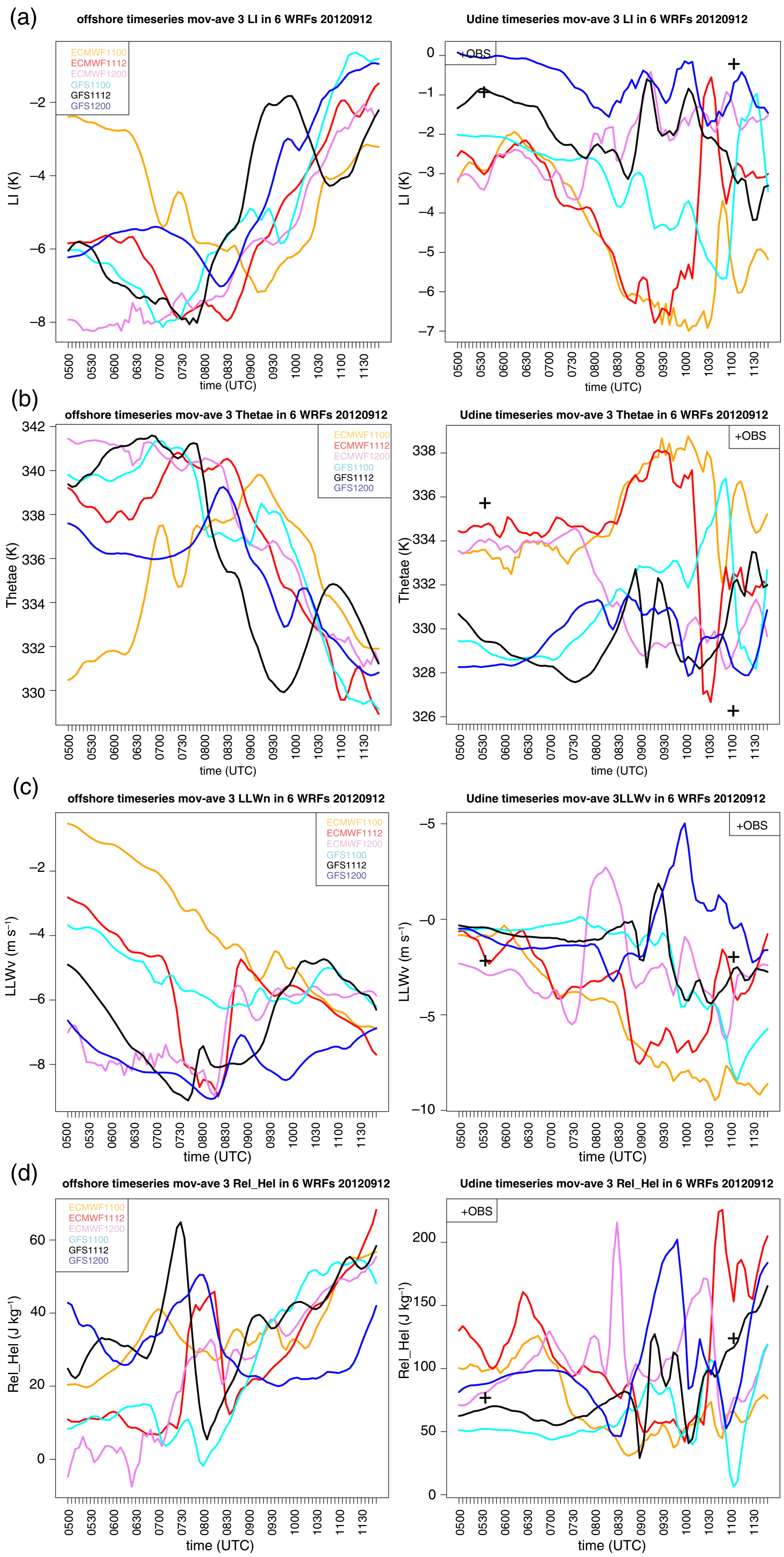

Figure 11. From top to bottom: 10 min moving average of (a) Lifted Index, (b) θ_e of the most unstable parcel, (c) low-level v-wind component and (d) Storm Relative Helicity, (left) offshore over the Adriatic Sea (45.4°N, 13.0°E) and (right) in the grid point closer to Udine (46.03°N, 13.18°E), between 0500 and 1200 UTC, 12 September 2012. Note that the 0600 (1200) UTC Udine (WMO 16044) sounding has been launched at 0526 (1059) UTC and has reached 500 hPa at 0545 (1116) UTC, so that the corresponding indices are plotted at 0535 (1105) UTC.

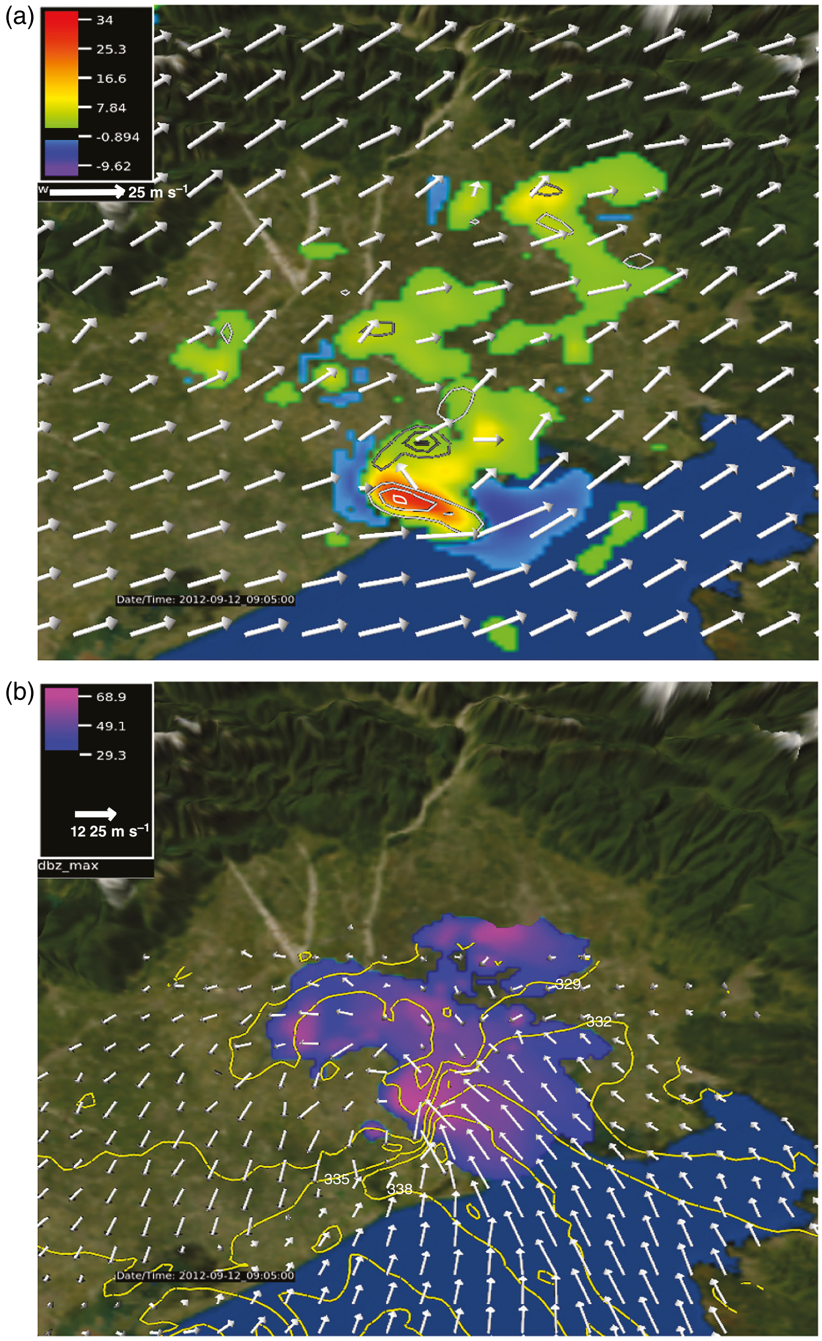

Figure 12. (a) Vertical velocity (shading; value between -1 and 1 m s^{-1} are not shown), vertical component of vorticity (contour interval 0.005 s^{-1}; black for negative values, white for positive, 0 not shown), and wind vectors at 5500 m, (b) Maximum reflectivity (shading; values below 30 dbZ are not shown), θ_e (contour interval 3 K; contours) and wind vectors at 100 m, simulated by the WRF model inner grid (GFS1112 run) at 0905 UTC 12 September 2012.

(apart from the left movers, as in Figure 4) and a significant degree of organized rotation around the updraught that persists for tens of minutes (Doswell and Burgess, 1993; Thompson, 1998). For the former, the simulated cell movement is from west-northwest to east-southeast, approximately coincident with the rain band elongation from Veneto toward Slovenia (Figure 2), and agrees well with the observations (cf. M15's Figure 5); thus, it is rightward of the average tropospheric wind shear, which in the morning of 12 September is approximately west-southwesterly (Figures 3 and 10). M15's Figure 13 confirms that the northern storm and the merged cell, as simulated in that article, have the rightward propagation typical of supercells. For the latter feature, the near superposition of the maxima of the vertical velocity and the vertical component of vorticity at 5500 m at 0905 UTC, 12 September (Figure 12(a)) is a typical feature of supercellular systems. Also, on the northern side of the cell, a small area of anticyclonic circulation is present, which can be associated with the splitting of the original cell (generated on the Alpine foothills at about 0600 UTC) induced by the downdraught, according to the conceptual model discussed in Rotunno (1981, his Figure 3) and Rotunno and Klemp (1982).

The structure of the cell at lower levels (Figure 12(b)) suggests that the intense rainfall induces strong evaporation contributing to the formation of a cold pool on the forward flank, which is crucial for the baroclinic generation of vorticity along the cold-air boundary and the low-level rotation of the system (Rotunno and Klemp, 1985). Also, the inflow of moist, potentially unstable low-level air from the Adriatic Sea that feeds the updraught is necessary to continuously trigger convection above the surface gust front. Such features are consistent with the conceptual model in Markowski and Richardson (2010)'s Figure 8.20. However, in the present case the supercell moves in synchronicity with the high-θ_e tongue; thus the evolution of the synoptic and mesoscale features appears to control its displacement. (In particular, its eastward movement follows the mesocyclone, while the southward movement corresponds to the intrinsic dynamics of a supercell.) While sharing a similarity with supercells forming on and moving with a dryline (Bluestein *et al.*, 2015), in the present case there is

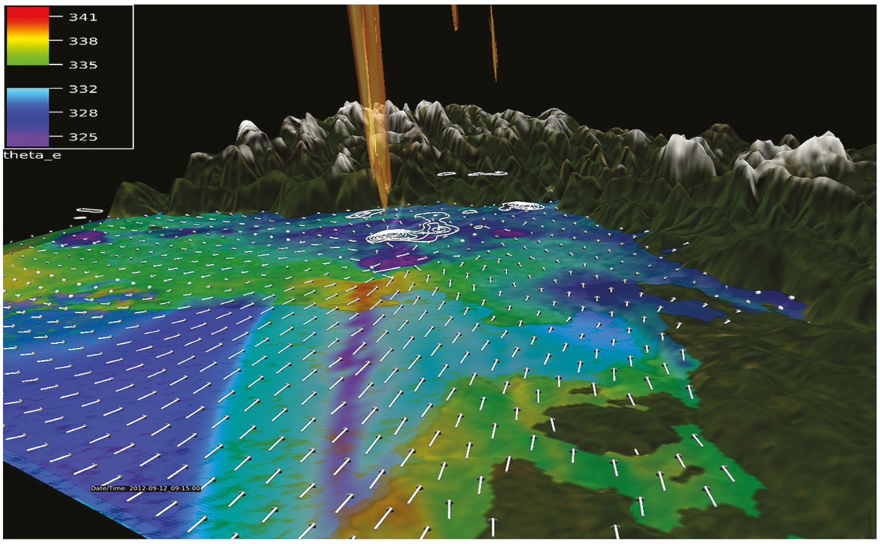

Figure 13. As Figure 7, but for GFS1112 run at 0915 UTC 12 September. The isosurface of $w = 12\,\mathrm{m\,s^{-1}}$ and rainwater content at 1000 m height (contour interval $1\,\mathrm{g\,kg^{-1}}$) are also shown.

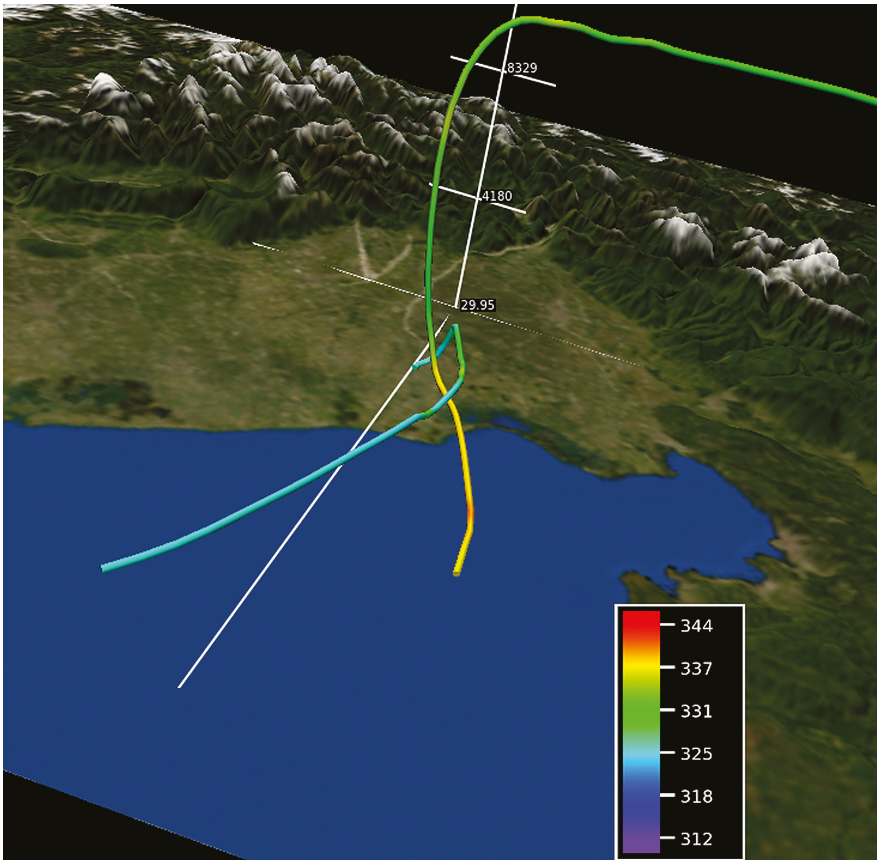

Figure 14. Two different trajectories wrapping around each other due to supercell rotation. The tones along the trajectories represent θ_e (in K).

also the low-level jet coming from the Adriatic Sea. As discussed in Feudale and Manzato (2014), the Adriatic Sea can be seen as a 'channel' formed by the Dinaric Alps and the Apennines. Wind can be channelized along the Sea while, on its northern side, the jet is influenced by the Alpine barrier, causing local convergence and inhomogeneity in the high-θ_e tongue, and thereby influencing the evolution of the supercell in way that appears qualitatively different from supercells over the US Great Plains.

A three-dimensional view during the mature stage of the cell is shown in Figure 13. The intense updraught (of more than $30\,\mathrm{m\,s^{-1}}$) is generated where the cold pool in the rear of the cell and the warm air inflow meet, a few km from the coast. The outflow associated with the downdraught is apparent, as well as the low-level rotation below the updraught. The high rainwater content assumes a bow-echo pattern, induced by the downward movement of the potentially cold mid-level air, which is further cooled down by the rainfall evaporation and moves underneath the low-level inflow.

The low-level rotation is more apparent in Figure 14, where two specific trajectories are shown. In agreement with Browning (1964)'s supercell model and with Klemp *et al.* (1981), the rear-flank updraught is created by ambient air entering the storm along the right (south) flank and then wrapped around the rear flank by the strengthening mesocyclone, while the forward-flank downdraught is wrapped around the north side of the updraught.

5. Conclusions

The present article focuses on a severe-convection episode occurring in Friuli Venezia Giulia (FVG, NE Italy) on the morning of 12 September 2012, during the Intensive Observation Period 2b (IOP2b) in the first Special Observation Period (SOP1) of the HyMeX campaign. One supercell, which produced hail and severe damage to trees and buildings, developed on the plain of FVG and was generated by the interaction between two previously existing cells.

Observations are analysed together with high-resolution WRF model simulations to identify the mechanisms responsible for the formation and development of the cell. Among six runs, starting from different large-scale forcing at different times, the simulation initialized at 1200 UTC, 11 September 2012 forced with GFS analysis/forecasts (GFS1112) is the one that best reproduces the observations which included a supercell thunderstorm.

The mesoscale features responsible for the event are well identified. Warm, moist air, mainly confined near the coast, is advected by a low-level jet toward the Prealps (Figure 2), producing large instability (although smaller than offshore) by increasing the local value of water-vapour mixing ratio, θ_e and *CAPE*; at the same time, an area of low-level convergence between the southerly inflow and a northeasterly barrier wind from the Alps favours convective triggering in the foothills; finally, cold air advection in the middle levels enhances potential instability.

A strong sensitivity to the initial and boundary conditions is demonstrated: only two of six simulations (GFS112 and GFS1100) were able to reproduce a persistent updraught rotation and the rightward movement typical of supercells; in two runs (ECM1100 and ECM1112), no precipitation is simulated along the coast, with rainfall generated by direct orographic uplift only near the Alps; in the other two runs (GFS1200 and ECM1200), the timing and the intensity of rainfall is far from that observed, and may possibly be affected by the model spin-up, since the triggering of convection started only a few hours after the initial condition. Considering that all the above experiments are undertaken in an operational-like mode, this result clearly shows that an ensemble approach (even a 'poor man' ensemble, as the one shown here) appears absolutely necessary to provide some indication on the risk of localized severe convective weather. Given a set of different simulations, a forecaster should consider the different outcomes emerging from an ensemble approach; in a nowcasting perspective, he/she should continuously follow the observations and give more credit to the model evolution remaining closer to them. From the preliminary experiments performed to identify an 'optimal' set-up and from the results in M15, the sensitivity to physics and to the limited-area model appears minor compared to that due to different larger-scale forcing and initial starting times, at least for this case. Also, due to the small horizontal scale of the supercell, a grid spacing of about 1 km is required for a proper simulation of this feature.

Another lesson that forecasters can learn from this work is that the occurrence of an – apparently – small low pressure above the Venice area can be considered as a warning signal for severe weather development. It seems that the successful simulation requires a deeper low in the Po Valley giving a farther inland penetration of deep ($\sim$500 m) low-level high-θ_e air, especially on the west side of the FVG plain, a weak (but non-zero) convective inhibition, necessary to confine the release of convection near the foothills, where the cold-air outflow plays an important role in the later evolution of the storm and, finally, low-level cold air confined near the mountains and the foothills. The latter point is very tricky, since cold air generally remains confined mainly in the narrow Alpine valleys, which are well below the resolution of a large-scale model. Unfortunately, the presence of a cold-air damming may easily be missed or misrepresented in the initial and boundary conditions. The significant climatological underestimation of the rainfall simulated by ECMWF forecasts in the FVG plain and coastal area during summer (Manzato *et al.*, 2016) is probably also a consequence of this kind of limitation.

The analysis of some instability parameters over the FVG plain and offshore (over the northern Adriatic Sea) before and during the event reveals significant small-scale variations in space and time, mainly as a consequence of the variations in the low-level θ_e. In particular, the sudden variations simulated in Udine are probably associated with the movement of the convective cells, which may temporary limit the tongue of warm air more to the south.

Lastly, supercell features emerging from the best simulation are consistent with the classical supercell model developed in Rotunno and Klemp (1985) mainly for US Plains supercells. However, while in the latter case the pattern of θ_e is generally homogeneous and stationary, in the present case the *synchronous movement of the high θ_e tongue with the cell* is a distinctive feature, which appears to be controlled mainly by mesoscale features. Also, the interaction of the moist and warm low-level jet with the Alps causes local convergence and inhomogeneity in the high-θ_e tongue (as shown also in Figure 1(b)), influencing the evolution of the supercell. The generality of these results should be tested extending a similar analysis to other Mediterranean events.

For future work, we plan to simulate the environment conducive to the present supercell in idealized conditions. In this way, we can systematically analyse the sensitivity of the solution to a range of values or to small perturbations added to the relevant parameters, in order to better understand the mechanisms that may have affected the triggering and development of the supercell, making apparent the differences with respect to the US supercell environment. Also, since the characteristics of the present supercell appear to have survived only for a short period (a few tens of minutes), the reason for such a short lifetime need to be analysed and discussed, possibly considering the role of the orography.

Acknowledgements

This work is a contribution to the HyMeX programme. Specials thanks go to Arturo Pucillo (OSMER-FVG) for Figure 1(a) and for his significant contribution to improve Figure 8. Stefano Zecchetto (ISAC-CNR) is gratefully acknowledged for Figure 1(b). Figures 7, 8, 12–14 were produced with VAPOR (http://www.vapor.ucar.edu). Figures 3, 4 and 5 are made with the NCAR Zebra software (Corbet *et al.*, 1994). The stay of R. Rotunno in Lecce was supported by the CNR short-term mobility programme; the stay of M. Miglietta in Boulder was supported by NCAR. We thank two anonymous reviewers for their helpful comments.

References

Bluestein HB, Snyder JC, Houser JB. 2015. A multiscale overview of the El Reno, Oklahoma, tornadic supercell of 31 May 2013. *Weather and Forecasting* **30**: 525–552.

Browning KA. 1964. Airflow and precipitation trajectories within severe local storms which travel to the right of the winds. *J. Atmos. Sci.* **21**: 634–639.

Bougeault P, Binder P, Buzzi A, Dirks R, Houze RA Jr, Kuettner J, Smith RB, Steinacker R, Volkert H. 2001. The MAP special observing period. *Bull. Am. Meteorol. Soc.* **82**: 433–462.

Corbet JM, Mueller C, Burghart C, Gould K, Granger G. 1994. ZEB: Software for integration, display and management of diverse environmental datasets. *Bull. Am. Meteorol. Soc.* **75**: 783–792.

Davolio S, Volonté A, Manzato A, Pucillo A, Cicogna A, Ferrario ME. 2016. Mechanisms producing different precipitation patterns over north-eastern Italy: Insights from HyMeX-SOP1 and previous events. *Q. J. R. Meteorol. Soc.*, doi: 10.1002/qj.2731.

Done JM, Craig GC, Gray SL, Clark PA, Gray MEB. 2006. Mesoscale simulations of organised convection: Importance of convective equilibrium. *Q. J. R. Meteorol. Soc.* **132**: 737–756.

Done JM, Craig GC, Gray SL, Clark PA. 2012. Case-to-case variability of predictability of deep convection in a mesoscale model. *Q. J. R. Meteorol. Soc.* **138**: 638–648, doi: 10.1002/qj.943.

Doswell CA III, Burgess DW. 1993. Tornadoes and tornadic storms: A review of conceptual models. In *The Tornado: Its Structure, Dynamics, Prediction, and Hazards*. *Geophysics Monographs*, Church C, Burgess DW, Doswell CA III, Davies-Jones R. (eds.), Vol. 79: 161–172. American Geophysical Union: Washington, DC.

Doswell CA III, Rasmussen EN. 1994. The effect of neglecting the virtual temperature correction on CAPE calculations. *Weather and Forecasting* **9**: 625–629.

Ducrocq V, Braud I, Davolio S, Ferretti R, Flamant C, Jansa A, Kalthoff N, Richard E, Taupier-Letage I, Ayral P-A, Belamari S, Berne A, Borga M, Boudevillain B, Bock O, Boichard J-L, Bouin M-N, Bousquet O, Bouvier C, Chiggiato J, Cimini D, Corsmeier U, Coppola L, Cocquerez P, Defer E, Delanoë J, Di Girolamo P, Doerenbecher A, Drobinski P, Dufournet Y, Fourrié N, Gourley JJ, Labatut L, Lambert D, Le Coz J, Marzano FS, Molinié G, Montani A, Nord G, Nuret M, Ramage K, Rison W, Roussot O, Said F, Schwarzenboeck A, Testor P, Van Baelen J, Vincendon B, Aran M, Tamayo J. 2014. HyMeX-SOP1: The field campaign dedicated to heavy precipitation and flash flooding in the northwestern Mediterranean. *Bull. Am. Meteorol. Soc.* **95**: 1083–1100.

Dudhia J. 1989. Numerical study of convection observed during the Winter Monsoon Experiment using a mesoscale two-dimensional model. *J. Atmos. Sci.* **46**: 3077–3107.

Feudale L, Manzato A. 2014. Cloud-to-ground lightning distribution and its relationship with orography and anthropogenic emissions in the Po Valley. *J. Appl. Meteorol. Clim.* **53**: 2651–2670.

Frei C, Schär C. 1998. A precipitation climatology of the Alps from high-resolution rain-gauge observations. *Int. J. Climatol.* **18**: 873–900.

Galway JG. 1956. The lifted index as a predictor of latent instability. *Bull. Am. Meteorol. Soc.* **37**: 528–529.

Giaiotti DB, Giovannoni M, Pucillo A, Stel F. 2007. The climatology of tornadoes and waterspouts in Italy. *Atmos. Res.* **83**: 534–541.

Isotta FA, Frei C, Weilguni V, Perčec Tadić M, Lassègues P, Rudolf B, Pavan V, Cacciamani C, Antolini G, Ratto SM, Maraldo L, Micheletti S, Bonati V, Lussana C, Ronchi C, Panettieri E, Marigo G, Vertačnik G. 2014. The climate of daily precipitation in the Alps: Development and analysis of a high resolution grid dataset from pan-Alpine rain-gauge data. *Int. J. Climatol.* **34**: 1657–1675, doi: 10.1002/joc.3794.

Janjić ZI. 2001. 'Nonsingular implementation of the Mellor–Yamada Level 2.5 Scheme in the NCEP Meso model,' NCEP Office Note 437. NCEP: College Park, MD.

Kain JS. 2004. The Kain–Fritsch convective parameterization: An update. *J. Appl. Meteorol.* **43**: 170–181.

Klemp JB, Wilhelmson RB, Ray PS. 1981. Observed and numerically simulated structure of a mature supercell thunderstorm. *J. Atmos. Sci.* **38**: 1558–1580.

Lilly DK. 1990. Numerical prediction of thunderstorm – Has its time come? *Q. J. R. Meteorol. Soc.* **116**: 779–798.

Manzato A. 2003. A climatology of instability indices derived from Friuli Venezia Giulia soundings, using three different methods. *Atmos. Res.* **67-68**: 417–454.

Manzato A. 2008. A verification of numerical model forecasts for sounding-derived indices above Udine, NE Italy. *Weather and Forecasting* **23**: 477–495.

Manzato A. 2012. Hail in NE Italy: Climatology and bivariate analysis with the sounding--derived indices. *J. Appl. Meteorol. Clim.* **51**: 449–467.

Manzato A, Morgan GM. 2003. Evaluating the sounding instability with the Lifted Parcel Theory. *Atmos. Res.* **67–68**: 455–473.

Manzato A, Davolio S, Miglietta MM, Pucillo A, Setvak M. 2015. 12 September 2012: A supercell outbreak in NE Italy? *Atmos. Res.* **153**: 98–118.

Manzato A, Cicogna A, Pucillo A. 2016. 6-hour maximum rain in Friuli Venezia Giulia: Climatology and ECMWF-based forecasts. *Atmos. Res.* **169B**: 465–484.

Markowski PM, Dotzek N. 2011. A numerical study of the effects of orography on supercells. *Atmos. Res.* **100**: 457–478.

Markowski P, Richardson Y. 2010. *Mesoscale Meteorology in Midlatitudes*. Wiley: New York, NY.

Marshall JS, Palmer WMK. 1948. The distribution of raindrops with size. *J. Meteorol.* **5**: 165–166.

Miglietta MM, Rotunno R. 2016. An EF3 multi-vortex tornado over the Ionian region: Is it time for a dedicated warning system over Italy? *Bull. Am. Meteorol. Soc.* **97**: 23–30.

Mlawer EJ, Taubman SJ, Brown PD, Iacono MJ, Clough SA. 1997. Radiative transfer for inhomogeneous atmosphere: RRTM, a validated correlated-k model for the longwave. *J. Geophys. Res.* **102**: 16663–16682, doi: 10.1029/97JD00237.

Niu G-Y, Yang Z-L, Mitchell KE, Chen F, Ek MB, Barlage M, Longuevergne L, Kumar A, Manning K, Niyogi D, Rosero E, Tewari M, Xia Y. 2011. The community Noah land surface model with multiparameterization options (Noah-MP): 1. Model description and evaluation with local-scale measurements. *J. Geophys. Res.* **116**: D12109, doi: 10.1029/2010JD015139.

Pucillo A, Manzato A. 2010. '08/08/08: The "Olympic storm" event and its implication about severe weather'. In *IV Hymex Workshop*, 8–10 June 2010. Bologna, Italy, p. 71 in Book of Abstracts of IV Hymex Workshop. http://www.hymex.org/public/workshops/4/BOOK_OF_ABSTRACT_HYMEX_2010.pdf?1407740830 (accessed 10 August 2016).

Punge HJ, Bedka K, Kunz M, Werner A. 2014. A new physically based stochastic event catalog for hail in Europe. *Nat. Hazards* **73**: 1625–1645.

Rotunno R. 1981. On the evolution of thunderstorm rotation. *Mon. Weather Rev.* **109**: 577–586.

Rotunno R, Klemp JB. 1982. The influence of the shear-induced pressure gradient on thunderstorm motion. *Mon. Weather Rev.* **110**: 136–151.

Rotunno R, Klemp JB. 1985. On the rotation and propagation of simulated supercell thunderstorms. *J. Atmos. Sci.* **42**: 271–292.

Schwartz CS, Romine GS, Sobash RA, Fossell KR, Weisman ML. 2015. NCAR's experimental real-time convection-allowing ensemble prediction system. *Weather and Forecasting* **30**: 1645–1654.

Skamarock WC, Klemp JB, Dudhia J, Gill DO, Barker DM, Duda M, Huang X-Y, Wang W, Powers JG. 2008. 'A description of the advanced research WRF Version 3'. NCAR Technical Note NCAR/TN–475+STR. NCAR: Boulder, CO.

Stensrud DJ, Xue M, Wicker LJ, Kelleher KE, Foster MP, Schaefer JT, Schneider RS, Benjamin SG, Weygandt SS, Ferree JT, Tuell JP. 2009. Convective-scale warn-on-forecast system: A vision for 2020. *Bull. Am. Meteorol. Soc.* **90**: 1487–1499, doi: 10.1175/2009BAMS2795.1.

Thompson RL. 1998. Eta model storm-relative winds associated with tornadic and nontornadic supercells. *Weather and Forecasting* **13**: 125–137.

Thompson G, Field PR, Rasmussen RM, Hall WD. 2008. Explicit forecasts of winter precipitation using an improved bulk microphysics scheme. Part II: Implementation of a new snow parameterization. *Mon. Weather Rev.* **136**: 5095–5115.

Weisman ML, Klemp JB. 1982. The dependence of numerically simulated convective storms on vertical wind shear and buoyancy. *Mon. Weather Rev.* **110**: 504–520.

Weisman ML, Davis C, Wang W, Manning KW, Klemp JB. 2008. Experiences with 0–36-h explicit convective forecasts with the WRF-ARW model. *Weather and Forecasting* **23**: 407–437.

Zhang F, Snyder C, Rotunno R. 2002. Mesoscale predictability of the 'surprise' snowstorm of 24–25 January 2000. *Mon. Weather Rev.* **130**: 1617–1632.

Zhang F, Snyder C, Rotunno R. 2003. Effects of moist convection on mesoscale predictability. *J. Atmos. Sci.* **60**: 1173–1185.